



# Room Temperature Operation of a Buried Heterostructure Photonic Crystal Quantum Cascade Laser

**Working Paper****Author(s):**

Peretti, Romain; Liverini, Valeria; Süess, Martin. J.; Liang, Yong; Vigneron, Pierre-Baptiste; Wolf, Johanna M.; Bonzon, Christopher; Bismuto, Alfredo; Metaferia, Wondwosen; Balaji, Manavaimaran; Lourudoss, Sebastian; Gini, Emilio; [Beck, Mattias](#) ; [Faist, Jérôme](#) 

**Publication date:**

2016

**Permanent link:**

<https://doi.org/10.3929/ethz-a-010711098>

**Rights / license:**

[In Copyright - Non-Commercial Use Permitted](#)

**Funding acknowledgement:**

317884 - Mid InfraRed Innovative lasers For Improved SENSor of hazardous substances (EC)

## Room Temperature Operation of a Buried Heterostructure Photonic Crystal Quantum Cascade Laser

R. Peretti<sup>1\*</sup>, V. Liverini<sup>1</sup>, M.J. Süess<sup>1</sup>, Y. Liang<sup>1</sup>, P.-B. Vigneron<sup>1</sup>, J. M. Wolf<sup>1</sup>, C. Bonzon<sup>1</sup>, A. Bismuto<sup>1</sup>, W. Metaferia<sup>2</sup>, B. Manavaimaran S.Lourdudoss<sup>2</sup>, E. Gini<sup>3</sup>, M. Beck<sup>1</sup> and J. Faist<sup>1</sup>

*"This is the pre-peer reviewed version of the following article: [Peretti, R., Liverini, V., Süess, M. J., Liang, Y., Vigneron, P.- B., Wolf, J. M., Bonzon, C., Bismuto, A., Metaferia, W., Balaji, M., Lourdudoss, S., Gini, E., Beck, M. and Faist, J. (2016), Room temperature operation of a deep etched buried heterostructure photonic crystal quantum cascade laser. Laser & Photonics Reviews. doi:10.1002/lpor.201600047], which has been published in final form at [ <http://dx.doi.org/10.1002/lpor.201600047> ]. This article may be used for non-commercial purposes in accordance with Wiley Terms and Conditions for Self-Archiving."*

*The authors advice to look at the final manuscript that included major improvements.*

\*Corresponding Author: perettir@phys.ethz.ch

<sup>1</sup>Institute for Quantum Electronics, ETH Zürich, 8093 Zürich, Switzerland

<sup>2</sup> Laboratory of Semiconductor Materials, School of ICT, KTH-Royal Institute of Technology, 164 40 Kista, Sweden.

<sup>3</sup>FIRST Center for Micro- and Nanoscience, ETH Zürich, 8093 Zürich, Switzerland

*Abstract: Getting high power single mode quantum cascade laser with a narrow far field is of importance for several applications including surgery or military countermeasure. Existing technologies suffer from drawbacks such as operation temperature or scalability. In this paper we demonstrate and characterize active region etched buried photonic crystal quantum cascade laser emitting around a wavelength of 8.5  $\mu\text{m}$ . The active region was dry etch before being regrown laterally with semi insulating Fe:InP. This fabrication strategy enabled to get refractive index contrast of 10% allowing good photonic mode control while keeping good thermal extraction during lasing operation. By performing photonic simulation, the measured lasing modes were identified as slow Bloch photonic crystal modes of a 550 $\mu\text{m}$  side square photonic crystal mesa. A peak power of 0.88 W at 263K with single mode behavior and narrow far field pattern was recorded. Lasing operation was measured at room temperature.*

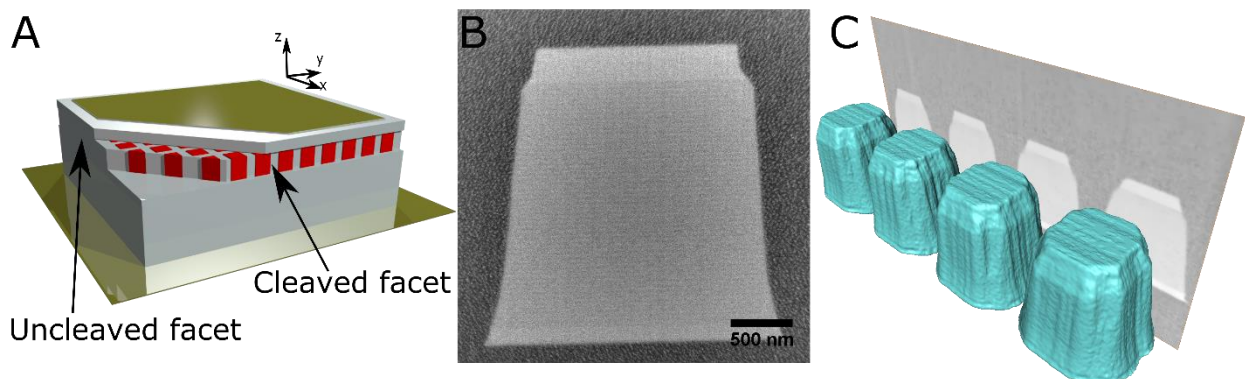
### 1. Introduction

Since the first demonstration of quantum cascades lasers (QCL) [1], these have become a well-established semiconductor laser source emitting in a wide wavelength range from mid-infrared to tera-hertz (THz). In the last decade the performance of QCLs was continuously improved by active region design and optimization, [2, 3] layer processing [4, 5] and laser mounting. [2, 6] Doubtlessly the recent advances in the understanding of optical losses [7] will improve even more their performance. Nowadays, QCLs are the most promising light source for many mid infra-red laser-based applications e.g. gas sensing, [8, 9, 10, 11] process control [12] and biological sensing. [13] Applications such as military counter measure, [14] photo acoustics [15, 16] or surgery, [17] which require specific high output power while keeping very good far field can be addressed by DFB [18] or MOPA [19, 20] technology. However, upscaling devices using these technologies is limited by appearance of multimode behavior when increasing the ridge cross section beyond laser wavelength or increasing the

device length. A promising approach to keep the coherence of a photonic mode on a large area is to use a two-dimensional (2D) periodic modulation of the refractive index at the scale of the wavelength, a so called photonic crystal (PhC). In the case of interband emitters, this strategy allows to keep excellent beam quality on large-surface area of lasers emitting large-power (3.5W) at room temperature (RT), while keeping a diffraction limited output beam [21]. PhCs allow to engineer losses and mode-active region overlap and thereby enable fine control of the mode selection. Two approaches were investigated for QCLs so far. On the one hand, air holes [22] and polymer separated pillars [23] PhC THz-QCLs were demonstrated at cryogenic temperature. But the use of plasmon modes either required THz gain active region or induced large losses preventing the laser to be operated at room temperature. On the other hand, in 2009, Bai et al. [24] proposed to use buried PhC distributed feedback structures on a large area (100  $\mu\text{m}$  x 3 mm) at 4.7  $\mu\text{m}$ . In fact, the distributed 2D grating allowed for high power (12W), RT operation and a diffraction limited far field. However, since the DFB PhC is only made from a low index contrast grating on top of the active region, its feedback remains relatively low and was even qualified as “*extremely weakly coupled system*”. [24] In fact increasing the coupling can be done by increasing the size of the sample and thus results in the emergence of unwanted modes due to its large area. This approach suffers then from the same scalability issue as the DFB cavities: parasitic modes reach laser threshold when device is too long. Hence, up to date no PhC-QCL with high coupling efficiency was operated at RT. In fact increasing the index contrast will ensure that the grating index modulation will remain higher than the ones due to any problem in the technology or to differences of temperature in the active region during operation.

Following the approach of buried heterostructures (BHs) proposed by Beck et al., [4] to manage loss and thermal dissipation, we present the design, fabrication and demonstration of a fully etched and buried active region PhC QCLs. These PhC QCLs provide strong photonic feedback due to refractive index contrast of about 10% while keeping a good thermal conduction and thus allow larger area QCLs with good far field. [4, 5] Consequently, we implemented a BH PhC QCL made of active region’s pillars surrounded by semi-insulating Fe doped InP as shown in **Figure 1** A, B and C.

**Figure 1:** A - Schematic of a BH PhC QCL mesa including buried photonic crystal of QCL active region (red), InP substrate (grey), top cladding (grey) and electrodes (gold). B - Scanning electron microscope image of a photonic crystal pillar exposed by focused ion beam (FIB) milling. C - 3D reconstruction of scanning electron microscope data recorded via FIB slice-and-view milling.

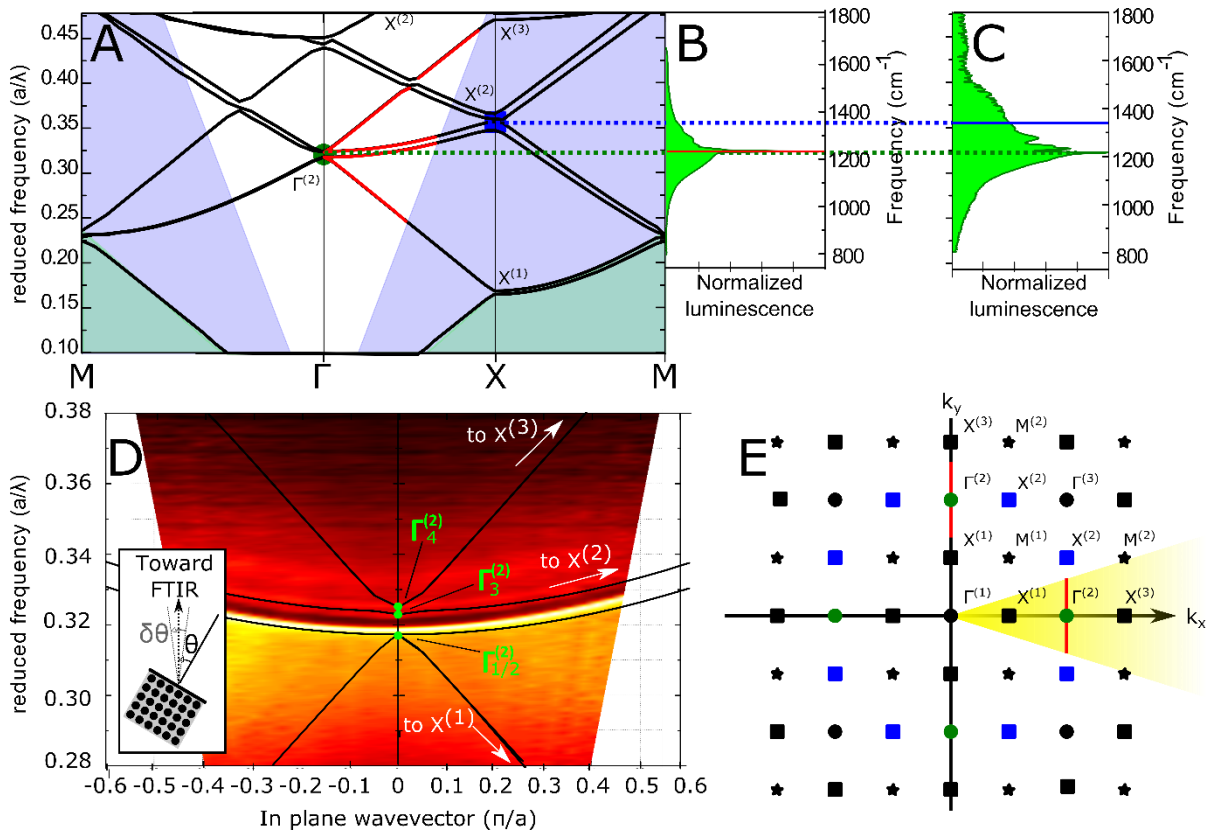


## 2. Experiments

Two active regions were grown, one based on lattice matched (LM) as described in [25], the other one, adapted from [26], on strain-compensated (SC) InGaAs/AlInAs material. Both are

aimed at to operate at around  $1200\text{ cm}^{-1}$  (see **figure 2 B & C**). The active regions are sandwiched by 100 nm thick InGaAs layers. The processed PhC-QCL mesas are shaped as square arrays of micropillars, of period “ $a$ ” around  $2.7\text{ }\mu\text{m}$  and width about  $2\text{ }\mu\text{m}$ . The pillars were processed using deep-UV lithography followed by ICP dry etching. [27] The space between the etched pillars was filled with semi-insulating Fe-doped InP using a low pressure Hydride vapour phase epitaxy. [28, 29, 27]. A Si doped InP top cladding was regrown using Metal Organic Vapour Phase Epitaxy (MOVPE). [27] The top electrodes were processed using e-beam evaporated Ti/Pt/Au layers (10nm/40nm/250nm) in a lift off process. The back electrode is an e-beam evaporated Ge/Au/Ni/Au layer (see figure 1 A). Focused ion beam was used to obtain sliced cross sections that were then analyzed by scanning electron microscopy and are shown in figure 1 B and C. The structural parameters extracted from this analysis, are the period,  $a = 2.7\text{ }\mu\text{m}$  and the areal filling factor of active regions  $\text{ff}=54\%$  (corresponding to 74% in distance). From the growth parameters, the height of the active region and InGaAs claddings together is 2.5 and 2.55  $\mu\text{m}$  for the LM and SC based structures, respectively. The epi-side up mounted on copper sub-mount sample consists of square mesa PhC-QCLs of 200 periods with  $\sim 550\text{ }\mu\text{m}$  side length. The samples were either uncleaved or cleaved on one, two or three facets along the x photonic crystal axis (see figure 1 A).

**Figure 2:** A) Computed band diagram, plotted along the  $\Gamma$ -X and  $\Gamma$ -M directions of the First Brillouin zone, plotted in reduced energy as a function of the in-plane wave vector. B) Electroluminescence spectrum taken with an FTIR spectrometer in scanning mode using an MCT detector and a lock-in amplifier. For the SC based device on the SC material, the spectrum was recorded at 250K, 1% duty cycle, 12.2A for the luminescence and 14A for the laser. Spectra are plotted as a function of reduced energy units to indicate the energy spectrum where gain is expected. The photon energy (in  $\text{cm}^{-1}$ ) is also indicated. The laser spectrum is indicated as a red line. C) Same data as B) but for the LM device, here the laser spectrum is denoted by a blue line. The luminescence spectrum was recorded at 200 K, 1% duty cycle, 3.5A for the luminescence and 4A for the laser. D) Experimental band diagram: normalized luminescence spectrum versus the in plane wave vector  $k_y$  (One spectrum was taken every  $10^\circ$  ( $\sim 0.01\pi/a$ )). The computed band diagram (black lines) around the lasing point is superimposed ( $T=15^\circ\text{C}$  period  $2.8\ \mu\text{m}$ , ff 50%, mesa  $550\ \mu\text{m}$ , Current 9.1A). Inset: Schematic of the measurement description (cleaved facet denoted in black). E) Unfolded Brillouin zone of the photonic crystal. The yellow triangle depicts the direct coupling “light-cone” toward a facet which is cleaved perpendicular to the x direction (see figure 1 A).



To analyze the modes supported by the PhC, three-dimensional (3D) finite difference time domain (FDTD) simulations were performed with the Lumerical software. [30] Bloch periodic conditions were used in the lateral direction while “perfectly matched layers” were used in the vertical direction. Refractive indices for InP (3.06) were taken from Palik [31]; for the active region (3.37) they were calculated as an average of the refractive indices of the individual active region materials weighted by their total thickness. After the simulation, the spectral properties (frequency, quality factor) of the modes were extracted from the temporal signal using a harmonic inversion methods (“projection” of the temporal trace on the family of the damped sinus functions; Harminv [32]) as in [33]. This resulted in a band diagram

plotted in figure 2 A. Here one can see that  $\Gamma^{(2)}$  k-point supports 3 modes all with sufficiently low horizontal losses to allow laser operation (cf. **table 1**) and  $X^{(2)}$  k-point 4 other ones. Figure 2 B and C show the active regions can provide gain for both family of modes in  $\Gamma^{(2)}$  and  $X^{(2)}$  k-points. However  $\Gamma^{(2)}$  modes have several advantages. First its frequency is at the maximum of the gain peak, second as shown on Figure 2 E where the facet emission cone defined by the Snell-Descartes law (the maximum angle is  $a.\sin(1/n_{mode})\sim 18^\circ$ ) is depicted in yellow, on the full Brillouin zone, this mode can be emitted through a facet. Lasing action was actually observed only on  $X^{(2)}$  for LM based device (see figure 2 C ) and on both k-points for the SC based devices (see figure 2 B ). The details about mode selection are discussed in [27]). To better understand this laser operation, spontaneous emission and laser spectrum are shown on the same figures. The amplified spontaneous emission spectrum contains four modes at  $1171\text{ cm}^{-1}$ ,  $1186\text{ cm}^{-1}$ ,  $1198\text{ cm}^{-1}$  and  $1228\text{ cm}^{-1}$ , situated around  $0.32\text{ a}^{-1}$ . This group of modes corresponds to modes originating from the crossing of bands at the  $\Gamma^{(2)}$  k-point. Similar measurements were done on SC samples. Again the amplified spontaneous emission spectrum contains four modes at  $1236\text{ cm}^{-1}$ ,  $1262\text{ cm}^{-1}$ ,  $1290\text{ cm}^{-1}$ ,  $1296\text{ cm}^{-1}$  located around  $0.32\text{ a}^{-1}$  at the  $\Gamma^{(2)}$  k-point.

To check if the parameters taken to calculate the frequency modes are accurate we measured the experimental band diagram shown on figure 2 D. In experiments, the variation of  $k_y$  vector corresponds to a variation of the angle  $\Theta$  between sample emission facet and the FTIR entrance axis. Normalized sub-threshold luminescence spectra recorded at different  $\Theta$  were plotted versus  $k_y = \sin(\Theta)2\pi/\lambda$ . To better illustrate the match between angles and k vectors, the span of  $k_y$  from figure 2 D is shown in Figure 2 A and 2E by red lines. In Figure 2A three branches can be seen: one from  $\Gamma^{(2)}$  to  $X^{(1)}$ , a double branch from  $\Gamma^{(2)}$  to  $X^{(2)}$  and the third from  $\Gamma^{(2)}$  to  $X^{(3)}$ . These paths can be seen in Figure. 2E where it is shown that only the double branch from  $\Gamma^{(2)}$  to  $X^{(2)}$  can directly couple toward a facet when the two other branches will need to use a lattice vector and thus couple less efficiently. The dispersion of the modes translates into a shift of the peak as a function of the observation angle. The resulting curves exhibit parabolic dispersion behaviour (non- linear dispersion term and curvature of  $0.036\text{ a}^{-1}/(\pi/a)^2$ ), a usual signature for a slow Bloch mode. For comparison, the band diagram of figure 2 A is superimposed. The good match between the experiments and the simulations shows the validity of the input parameters of the simulation. The superposition shows as well that the two modes forming the gap are the modes  $\Gamma_{1/2}^{(2)}$  and  $\Gamma_3^{(2)}$ . Since the lasing action occurred on the mode with the lowest energy (see figure 2 C), the lasing mode is unambiguously identified as  $\Gamma_{1/2}^{(2)}$ . In addition, the bands from  $\Gamma^{(2)}$  to  $X^{(2)}$  are visible in the experimental data, but not those from  $\Gamma^{(2)}$  to  $X^{(1)}$  or  $X^{(3)}$ , which is explained by the fact that the band to  $X^{(2)}$  can couple directly through a facet cleaved perpendicular to x (see figure 1 A), but the one to  $X^{(1)}$  or  $X^{(3)}$  only helped by a grating vector (cf. figure 2 E).

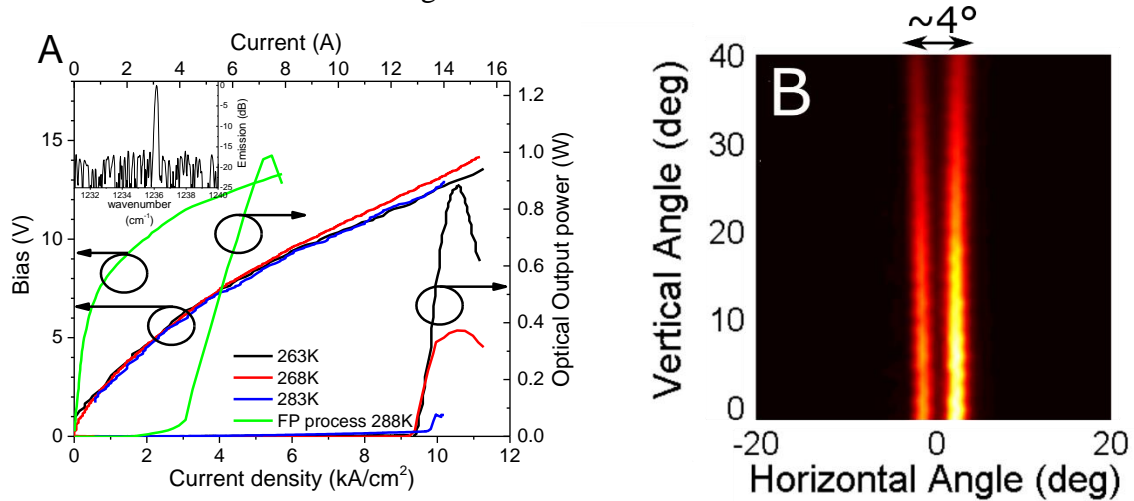
To better understand why the  $\Gamma_{1/2}^{(2)}$  lases predominantly, 3D-FDTD simulations were conducted using the structural information extracted from the FIB measurement displayed in figure 2 C in order to quantify the modal losses and overlap factors taking into account the vertical confinement by calculating the field distribution of each mode (cf. Table 1). In addition, the horizontal losses were evaluated by computing 2D simulations of finite size sample (200 periods) in both x and y directions surrounded by “perfect match layer” (absorbing boundary conditions) on each side of the PhC for the case of uncleaved facet and for the case of only one cleaved facet.

**Table 1:** Spectral properties of the simulated modes, the symmetries name are taken from [34]

	Frequency [cm <sup>-1</sup> ]	Wavelength [μm]	Vert. Losses [cm <sup>-1</sup> ]	Horiz.Losses 0 cleaved facet [cm <sup>-1</sup> ]	Horiz. Losses 1 cleaved facet [cm <sup>-1</sup> ]	Overl ap factor	Symmetry
$\Gamma_{1/2}^{(2)}$	1196	8.4	0.50	18	5	0.44	E
$\Gamma_3^{(2)}$	1218	8.2	<0.1	3.6	2.3	0.28	A1
$\Gamma_3^{(2)}$	1226	8.2	<0.1	<0.1	<0.1	0.24	B1

At the  $\Gamma^{(2)}$  k-point the simulations for infinite structures predict modes with very low radiative vertical losses compared to free carrier absorption (FCA) ( $\sim 4 \text{ cm}^{-1}$ ) and thus to the actual losses in the device. Hence, vertical losses cannot play any role in the mode selection. The computed horizontal losses are closer to or even higher than those of FCA and will play a role in the selection process. Furthermore, cleaving a facet is of prime importance for mode  $\Gamma_{1/2}^{(2)}$  for which the lateral losses are lower by a factor  $\sim 3$  due to reflectivity on the facet. Moreover  $\Gamma_{1/2}^{(2)}$  mode has the highest overlap factor among all the modes in  $\Gamma^{(2)}$ , which has a twofold effect. First, the gain is higher than the one imparted to other modes at the same voltage. Second, a better 3D confinement improves the waveguide confinement due to higher effective index contrast. This directly impacts how the mode interacts with the top electrode (metal and highly doped region) as in [35]. Modes with high overlap experience less losses from the top electrode. All in all, since the actual losses are the sum of the PhC losses and the absorption losses (both the FCA and the top electrode ones), laser operation occurs at mode  $\Gamma_{1/2}^{(2)}$  because its higher gain and lower absorption losses will surpass the non-radiative losses when the sample is cleaved.

**Figure 3** : A: LIV curve for a PhC laser and FP laser of the same structure (SC based lasers): the current-voltage curve uses the left ordinate and the light-current curve the right ordinate). PhC laser characteristics: period=2.6  $\mu\text{m}$ , ff=54%, 530  $\mu\text{m}$  mesa; FP characteristics: 3 mm long and 8.5  $\mu\text{m}$  wide. For both cases: Duty cycle 0.025% and repetition rate 2.5 kHz. Inset spectrum of the PhC laser at 263K and 14A. B: Far field patterns of the lasing modes  $\Gamma_{1/2}^{(2)}$  of PhC. The horizontal angle rotation is the rotation around axe z.



The power-current-voltage (LIV) characteristics of an SC laser were recorded at a repetition rate of 2.5 kHz and a duty cycle of 0.025% (figure 3 A). The power was measured with a liquid nitrogen cooled MCT detector (using a density filter while needed) and calibrated with a power meter. The characteristics of an uncoated 3 mm long 8.5 $\mu\text{m}$  wide Fabry-Perot (FP) device from the same MBE growth (recorded at 288K) with similar process as [5, 25] are plotted in the same figure, in order to compare to the threshold losses of the BH PhC devices. The Bias and current density scale are the same but current and power axes in are not to scale for the FP device. The facet emitting mode  $\Gamma_{1/2}^{(2)}$  reaches peak powers of up to 0.88 W. The IV curves show some leakage in the PhC process compared to the FP laser of the same structure. This effect is most pronounced in the SC based devices, where typical threshold currents around 9.7 $\text{kA}/\text{cm}^2$  are observed, in contrast to 3 $\text{kA}/\text{cm}^2$  for the LM based devices (instead of 2.7  $\text{kA}/\text{cm}^2$  around 270K for SC based device and 2.5 $\text{kA}/\text{cm}^2$  at 250K for LM based device, see [27] electrical characterisation)). This difference can be explained by the fact that the growth rate at the beginning of the lateral regrowth of InP:Fe was higher than targeted for the SC process. This can possibly lead to an incomplete incorporation of iron. In addition, the voltage at threshold is about 1V higher in the case of PhC process. Since voltage should not depend as much on leakage, the voltage offset is attributed to higher losses of PhCs compared to FP process.

A far field pattern recorded on a PhC sample from the SC process is shown in figure 3 B. The horizontal and vertical angles correspond to rotations around the z- and x-axes displayed in figure 1 A, respectively. The mode at  $\Gamma_{1/2}^{(2)}$  shows two narrow lobes. The full width at half maximum corresponds to the resolution limit of the setup coinciding with the diffraction limited low spatial-frequencies pass filter of a 550  $\mu\text{m}$  long facet ( $\sim 1.8^\circ$ ). The two lobes are separated by a divergence angle of about  $4^\circ$ . The  $\Gamma_{1/2}^{(2)}$  mode coupling to a facet has a k-vector perpendicular to it (see figure 2 E). This means that the phase of the wave on this facet is not modulated by the Bloch mode of the PhC. Thus the only way to get a modulation giving rise to double lobe behaviour is a modulation by the envelope of the PhC Bloch mode.



Considering the angle between the two lobes; this corresponds to the diffraction limited emission of the second order lateral mode (i.e. antisymmetric mode with respect to the centre of the emission facet). The spectral difference between this mode and the fundamental mode is  $\sim 0.01\text{cm}^{-1}$  which cannot be resolved with our apparatus, however the far field pattern clearly shows single mode behaviour (further explanation is given in [27]). The broad angle in the vertical direction corresponds to the diffraction limited angle through a  $3\ \mu\text{m}$  thick slit (thickness of the active region).

### 3. Conclusion

In summary, we designed, fabricated and analysed PhC QCLs that lase at 2 different symmetry points of the Brillouin zone depending on the number of cleaved facets. Heat extraction was optimized by a buried heterostructure process protocol with InP:Fe regrowth between the PhC pillars, which allows room temperature operation for both investigated processes. Highest performance was achieved for a  $> 550\ \mu\text{m} \times 550\ \mu\text{m}$  QCL lasing at single mode with  $0.88\ \text{W}$  output power per facet. Despite the current leakage and the optical losses, the laser reaches already high output peak power with a narrow emission pattern. Our approach based on etched active region provides about 10% of refractive index contrast and an improved selectivity due to spatial gain modulation we were then able to maintain single mode behaviour while getting such high power. These characteristics will thus be very useful in application such as military countermeasures or photoacoustic detection. Hence it is promising for future realizations of electrically injected buried PhC lasers, which will finally pave the way for large area high power single mode QCLs.

**Acknowledgements** This work was supported by EU FP7 MIRIFISENS Integrated Project 317884 and the Swedish Research Council (VR) through the grant proposal 2015-05470 and Linné Center of Excellence, ADOPT.

**Keywords:** quantum cascade laser, photonic crystal, mid infrared, single mode

### References

- [1] J. FAIST, F. CAPASSO, D.L. SIVCO, C. SIRTORI, A.L. HUTCHINSON, and A.Y. CHO, *Science* **264**(5158), 553–556 (1994).
- [2] A. LYAKH, R. MAULINI, A. TSEKOUN, R. GO, C. PFLÜGL, L. DIEHL, Q.J. WANG, F. CAPASSO, and C.K.N. PATEL, *Applied Physics Letters* **95**(14), – (2009).
- [3] A. BISMUTO, R. TERAZZI, B. HINKOV, M. BECK, and J. FAIST, *Applied Physics Letters* **101**(2), 021103 (2012).
- [4] M. BECK, J. FAIST, U. OESTERLE, M. ILEGEMS, E. GINI, and H. MELCHIOR, *Photonics Technology Letters, IEEE* **12**(11), 1450–1452 (2000).
- [5] M. BECK, D. HOFSTETTER, T. AELLEN, J. FAIST, U. OESTERLE, M. ILEGEMS, E. GINI, and H. MELCHIOR, *Science* **295**(5553), 301–305 (2002).
- [6] K. FUJITA, S. FURUTA, A. SUGIYAMA, T. OCHIAI, A. ITO, T. DOUGAKIUCHI, T. EDAMURA, and M. YAMANISHI, *Applied Physics Letters* **98**(23), – (2011).
- [7] C. NDEBEKA-BANDOU, A. WACKER, F. CAROSELLA, R. FERREIRA, and G. BASTARD, *Applied Physics Express* **6**(9), 094101 (2013).
- [8] J. HODGKINSON and R.P. TATAM, *Measurement Science and Technology* **24**(1), 012004 (2013).
- [9] J. LI, U. PARCHATKA, and H. FISCHER, *Sensors and Actuators B: Chemical* **182**, 659–667 (2013).
- [10] J. JÁGERSKÁ, P. JOUY, A. HUGI, B. TUZSON, H. LOOSER, M. MANGOLD, M. BECK, L. EMMENEGGER, and J. FAIST, *Applied Physics Letters* **105**(16), 161109 (2014).
- [11] Y. WANG, M.G. SOSKIND, W. WANG, and G. WYSOCKI, *Applied Physics Letters* **104**(3) (2014).

- [12] N. LANG, J. RÖPCKE, S. WEGE, and A. STEINBACH, *The European Physical Journal Applied Physics* **49**(01), 13110 (2010).
- [13] A. REYES-REYES, R.C. HORSTEN, H.P. URBACH, and N. BHATTACHARYA, *Analytical Chemistry* **87**(1), 507–512 (2015), PMID: 25506743.
- [14] A. SIJAN, Development of military lasers for optical countermeasures in the mid-ir, in: *SPIE Europe Security+ Defence*, (2009), pp.748304–748304.
- [15] V. SPAGNOLO, P. PATIMISCO, S. BORRI, G. SCAMARCIO, B. BERNACKI, and J. KRIESEL, *Applied Physics B* **112**(1), 25–33 (2013).
- [16] T. BERER, M. BRANDSTETTER, A. HOCHREINER, G. LANGER, W. MÄRZINGER, P. BURGHOLZER, and B. LENDL, *Optics letters* **40**(15), 3476–3479 (2015).
- [17] K. HASHIMURA, K. ISHII, N. AKIKUSA, T. EDAMURA, H. YOSHIDA, and K. AWAZU, *Journal of Innovative Optical Health Sciences* **7**(03), 1450029 (2014).
- [18] Q.Y. LU, Y. BAI, N. BANDYOPADHYAY, S. SLIVKEN, and M. RAZEGHI, *Applied Physics Letters* **98**(18), – (2011).
- [19] B. HINKOV, M. BECK, E. GINI, and J. FAIST, *Opt. Express* **21**(16), 19180–19186 (2013).
- [20] S. MENZEL, L. DIEHL, C. PFLÜGL, A. GOYAL, C. WANG, A. SANCHEZ, G. TURNER, and F. CAPASSO, *Optics express* **19**(17), 16229–16235 (2011).
- [21] K. HIROSE, Y. LIANG, Y. KUROSAKA, A. WATANABE, T. SUGIYAMA, and S. NODA, *Nature Photonics* **8**(5), 406–411 (2014).
- [22] R. COLOMBELLI, K. SRINIVASAN, M. TROCCOLI, O. PAINTER, C.F. GMACHL, D.M. TENNANT, A.M. SERGENT, D.L. SIVCO, A.Y. CHO, and F. CAPASSO, *Science* **302**(5649), 1374–1377 (2003).
- [23] Z. DIAO, C. BONZON, G. SCALARI, M. BECK, J. FAIST, and R. HOUDRÉ, *Laser & Photonics Reviews* **7**(5), L45–L50 (2013).
- [24] Y. BAI, B. GOKDEN, S.R. DARVISH, S. SLIVKEN, and M. RAZEGHI, *Applied Physics Letters* **95**(3), – (2009).
- [25] A. BISMUTO, R. TERAZZI, M. BECK, and J. FAIST, *Applied Physics Letters* **96**(14), 141105 (2010).
- [26] A. LYAKH, R. MAULINI, A. TSEKOUN, R. GO, and C.K.N. PATEL, *Opt. Express* **20**(22), 24272–24279 (2012).
- [27] Please see supporting information.
- [28] W. METAFERIA, B. SIMOZRAG, C. JUNESAND, Y.T. SUN, M. CARRAS, R. BLANCHARD, F. CAPASSO, and S. LOURDUDOSS, *Optical Engineering* **53**(8), 087104–087104 (2014).
- [29] S.LOIRDUDOSS, W. METAFERIA, C. JUNESAND, B. MANAVAIMARAN, S. FERRÉ, B. SIMOZRAG, M. CARRAS, R. PERETTI, V. LIVERINI, M. BECK, and J.FAIST, Hydride vapour phase epitaxy assisted buried heterostructure quantum cascade lasers for sensing applications, in: *SPIE photonic WEST : Quantum Sensing and Nanophotonic Devices XII*, (2015).
- [30] [HTTP://WWW.LUMERICAL.COM/](http://www.lumerical.com/).
- [31] E.D. PALIK, *Handbook of Optical Constants of Solids: Index* (Academic press, 1998).
- [32] V. MANDELSHTAM, *Progress in Nuclear Magnetic Resonance Spectroscopy* **38**(2), 159 (2001).
- [33] R. PERETTI, C. SEASSAL, P. VIKTOROVICH, and X. LETARTRE, *Journal of Applied Physics* **116**(2), – (2014).
- [34] K. SAKODA, *Optical properties of photonic crystals* (Springer, 2001).
- [35] C. SIRTORI, C. GMACHL, F. CAPASSO, J. FAIST, D.L. SIVCO, A.L. HUTCHINSON, and A.Y. CHO, *Opt. Lett.* **23**(17), 1366–1368 (1998).